PUSHER PROPELLER NON-HARMONIC ACTUATION FOR ACTIVE VIBRATION CONTROL

Henry F. Malarkey V †
Graduate Research Assistant

Edward C. Smith
Professor

Sven U. Schmitz
Professor

Jianhua Zhang
Assist. Research Professor

The Pennsylvania State University, *University Park, Pennsylvania, USA*

Matthew W. Floros
Aerospace Engineer
DEVCOM Army Research Laboratory
Aberdeen Proving Ground, Maryland, USA

ABSTRACT

The vibration control authority for coaxial rotor higher harmonic control (HHC) and a new pusher propeller active vibration control (AVC) system was evaluated with the Rotorcraft Comprehensive Analysis System (RCAS) coupled with the Viscous Vortex Particle Method (VVPM). Model refinements were implemented, and cockpit vibration predictions were validated against available flight test data, despite inconsistencies in the literature. A closed-loop HHC study for the XH-59A coaxial rotor predicted a maximum HHC pitch requirement of 2.3°. The theoretical basis for the pusher propeller AVC system was established by modulating steady pusher propeller hub loads at harmonics of the main coaxial rotor, even though the propeller rotates at a non-harmonic speed. A pusher propeller appended to the XH-59A model demonstrated the concept's feasibility in four stages.

NOMENCLATURE

$\langle x,y,z \rangle$	Position, ft
$\langle \dot{x},\dot{y},\dot{z} \rangle$	Velocity, ft/s
$\langle \ddot{x},\ddot{y},\ddot{z} \rangle$	Acceleration, ft/s^2
A	AVC pitch amplitude, deg
H	Rotor longitudinal force (positive aft), lb
II	Intrusion index
k	Blade index
LOS	Lift offset
M_x	Rotor rolling moment, ft-lb
M_y	Rotor pitching moment, ft-lb
N	Number of blades
N_F	Blade root flapwise moment, ft-lb
N_L	Blade root lagwise moment, ft-lb
N_R	Nominal rotor speed of rotation, rad/s
Q	Rotor torque, ft-lb
R	Rotor radius, ft
S_x	Blade root lagwise shear force, lb
S_z	Blade root vertical shear force, lb
T	Rotor thrust, lb
Y	Rotor lateral force (positive starboard), lb
Γ	Swashplate phase angle, rad/s
Θ	Coaxial rotor controls, deg
θ	Blade pitch, deg
ϕ	AVC phase, deg
ψ	Rotor azimuth, deg
Ω	Rotor speed of rotation, rad/s
$\Delta()$	Differential quantity
$()^{MR}$	Main coaxial rotor quantity
$()^{U}$	Upper rotor quantity
$()^{L}$	Lower rotor quantity
$()^{PP}$	Pusher propeller quantity
$()_n$	n/rev harmonic amplitude
$()_{nc}$	n/rev cosine component
$()_{ns}$	n/rev sine component

AVC	Active Vibration Control
BEMT	Blade Element Momentum Theory
CG	Center of Gravity
HHC	Higher Harmonic Control
IBC	Individual Blade Control
RCAS	Rotorcraft Comprehensive Analysis System
VVPM	Viscous Vortex Particle Method

†Corresponding author: hfm5358@psu.edu

Presented at the 51st European Rotorcraft Forum, Venice, Italy, September 9–12, 2025.

INTRODUCTION

Modern missions necessitating high speed could be accomplished by stiff, hingeless, lift-offset coaxial rotorcraft, but they are hindered by intense vibratory hub loads. For such aircraft, an active vibration control (AVC) system is no longer optional: it is a necessity — unlike traditional helicopters, where passive vibration control is sufficient. Modern coaxial compound vehicles use fuselage force generators, which are effective but impose a substantial weight penalty, limiting both payload and range (Ref. 1). Two AVC alternatives are higher harmonic control (HHC), with actuators in the non-rotating frame (Ref. 2), and individual blade control (IBC), with actuators in the rotating frame (Ref. 3). Over seven decades of research (Ref. 4) have demonstrated the vibration reduction, noise attenuation, in-flight blade tracking, and performance improvement capabilities of these blade-actuated AVC systems. However, reluctance to adopt the technology persists due to the safety-critical reliability requirements of such systems, as well as manufacturing and maintenance costs (Refs. 2, 3). In particular, IBC via pitch link actuators is complicated by hydraulic slip rings and has limited usable piston stroke, about 1–2° effective pitch (Ref. 5). Hence, this work focuses on two primary objectives:

1. Reevaluate the feasibility of main coaxial rotor HHC for vibration reduction with modern comprehensive analysis

2. Investigate an alternative that is lighter, simpler, and less safety-critical: pusher propeller AVC

LITERATURE REVIEW

In a thorough survey of HHC and IBC presented at the 36th European Rotorcraft Forum in 2010, Kessler summarized the state of the field at the time,

> "About 58 years of research and development on HHC and IBC have passed by. And no helicopter is equipped with such a system. More years will even pass by." (Ref. 3)

He argued that research efforts were unfocused with too many competing concepts for such a complex problem. He also noted that HHC/IBC may not be economically viable for conventional helicopters where vibration and noise levels are tolerable, albeit a nuisance. Although the years have continued to pass without commercial implementation, focused research has since emerged to quantify the effectiveness of HHC/IBC for stiff, lift-offset coaxial rotorcraft, which require AVC.

The foundation for the present work dates back to a 1980 design analysis of HHC for the Sikorsky XH-59A (Ref. 6), depicted in Fig. 1 with specifications in Table 1. It explained that counter-rotating coaxial rotors are ideal candidates for fixed-frame HHC because the symmetry of the configuration reduces the dimensionality of the hub loads in a reference frame set by the crossover angle. Crossover angle — an azimuth position where the upper and lower rotor blades pass one another — defines the mechanically-linked relative position of the rotors. Their analysis required a maximum of 2° HHC actuation to reach acceptable vibration levels. Subsequent progress began in 2015, when Jacobellis developed a Rotorcraft Comprehensive Analysis System (RCAS) model of the XH-59A (Ref. 7), based primarily off of specifications published in Ruddell's technology demonstrator reports (Refs. 8, 9) and Felker's wind tunnel test report (Ref. 10). During the same time, Lee and Park independently developed a similar XH-59A model in CAMRAD II, but with the addition of an MSC.NASTRAN elastic fuselage that they used to compare fuselage force generators and main coaxial rotor IBC (Ref. 11). Beyer et al. then obtained Jacobellis' isolated rotor model and implemented main rotor IBC, performing open and closed-loop studies (Ref. 12). In 2024, Zhang et al. repeated Beyer's studies with a higher fidelity aerodynamic model, the Viscous Vortex Particle Method (VVPM) (Refs. 13,14), which captured significant $6/\text{rev}^{MR}$ hubs loads caused by rotor-rotor interference in addition to $3/\text{rev}^{MR}$ hub loads (Ref. 15). Finally, Mawry et al. collaborated with Park to incorporate his group's elastic fuselage into a coupled rotor-fuselage RCAS model, which altered hub loads and proved essential for assessing IBC effectiveness (Ref. 16). Note that these studies on IBC for vibration reduction could also be accomplished with HHC actuation, which is explained in more detail in the following sections.

Figure 1: XH-59A (Ref. 17)

Table 1: XH-59A Specifications

Gross Weight	12 500 lb
Fuselage Length	40 ft 8 in
Rotor Radius	18 ft
Blades / Rotor	3
Nominal Rotation Speed	345 RPM
Rotor Crossover	0°
Blade Pre-cone	3°
Root Cutout	10%R
Shaft Tilt	0°
Rotor Separation	30 in
CG Location[a]	5.3 in fore & 42 in below
Power Plant	2 × P&W[b] PT6-3
Auxiliary Propulsion	2 × P&W[b] J60-P3A

[a]Referenced to the lower rotor [b]P&W: Pratt & Whitney

MODEL REFINEMENTS

Building upon the work of Mawry et al. (Ref. 16), several model refinements were made to the XH-59A RCAS model

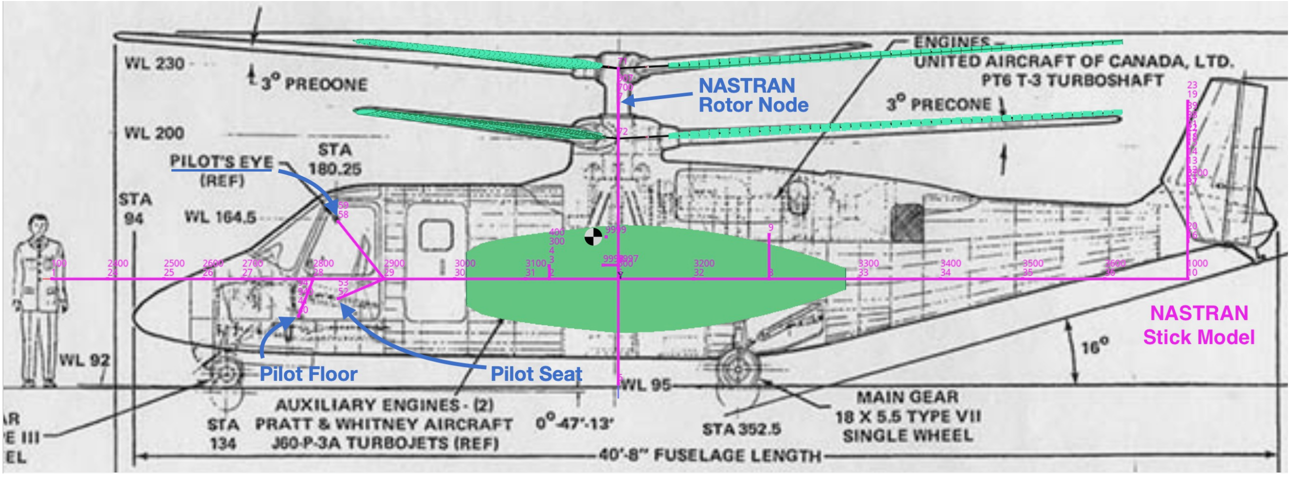

Figure 2: NASTRAN Stick Model Overlay with Rigid Bar Extrapolations (background image from Ref. 8)

to improve the accuracy of our AVC predictions. First, the aerodynamic model fidelity was increased from a prescribed wake to the VVPM. Compared to the VVPM work on the isolated main coaxial rotor (Ref. 15), the number of aerodynamic segments and VVPM spanwise particle resolution were increased, and bound circulation interference was enabled. Next, rigid bars were added to extrapolate the vibratory response of the elastic fuselage stick model to the pilot and copilot seat and floor locations, visible in Fig. 2. This extrapolation linearly approximates the increase or decrease in vibration response, depending on phase, caused by rotational vibrations acting on the offset locations from the elastic joint connection.

To quantify the vibrations at these new locations, the intrusion index was calculated. The intrusion index, defined in ADS-27A-SP (Ref. 18), is a weighted Euclidean norm of the local longitudinal, side, and vertical vibratory velocity spectra, in inches per second, with weights dependent on frequency. For simplicity, ADS-27A-SP includes only the largest weighted peaks, four per direction, in the calculation, and the acceptable intrusion index limits are specified to be 1.2 for pilots and 1.0 for weapon system operators. However, to assess vibrations at specific frequencies for the XH-59A, a separate $3/\text{rev}^{MR}$ (16.9 Hz) intrusion index component was used,

$$II_3 = \sqrt{(\dot{x}_3/0.68)^2 + (\dot{y}_3/0.51)^2 + (\dot{z}_3/0.34)^2} \quad (1)$$

In Figs. 3, 12, 13, & 14 that plot cockpit vibrations, solid lines represent the pilot floor location, and dashed lines represent the copilot floor location.

For the last refinement, the closed-loop optimization algorithm was changed from Newton-Raphson to a Broyden trust region quasi-Newton method, which offers improved robustness to system nonlinearity (Ref. 19).

TRIM & BASELINE COCKPIT VIBRATION VALIDATION

Aircraft trim was achieved using the coaxial rotor controls defined in Table 2, which are expressed in terms of the separate controls for the upper and lower rotors:

Table 2: Main Coaxial Rotor Controls

Mean Collective	$\Theta_0 = \frac{1}{2}\left(\theta_0^U + \theta_0^L\right)$
Differential Collective	$\Delta\Theta_0 = \frac{1}{2}\left(\theta_0^U - \theta_0^L\right)$
Mean Lateral	$\Theta_{lat} = \frac{1}{2}\left(\theta_{lat}^U + \theta_{lat}^L\right)$
Differential Lateral	$\Delta\Theta_{lat} = \frac{1}{2}\left(\theta_{lat}^U - \theta_{lat}^L\right)$
Mean Longitudinal	$\Theta_{long} = \frac{1}{2}\left(\theta_{long}^U + \theta_{long}^L\right)$
Differential Longitudinal	$\Delta\Theta_{long} = \frac{1}{2}\left(\theta_{long}^U - \theta_{long}^L\right)$

$$\theta^U = \theta_0^U + \theta_{lat}^U \sin(\psi^{MR} + \Gamma) + \theta_{long}^U \cos(\psi^{MR} + \Gamma) \quad (2)$$

$$\theta^L = \theta_0^L + \theta_{lat}^L \sin(\psi^{MR} + \Gamma) + \theta_{long}^L \cos(\psi^{MR} + \Gamma) \quad (3)$$

Here, ψ^{MR} is defined in the direction of rotation for each rotor so that $\psi^{MR} = 90°$ is always on the advancing side. Due to the stiff blades on the XH-59A, there is a small phase lag of 30° in flap response (Ref. 8), which is accounted for by the swashplate phase angle, Γ.

Trim targets included setting the differential lateral control to reach a specified lift-offset value, defined as

$$LOS = \frac{\Delta M_x^{MR}}{T^{MR} R^{MR}} \quad (4)$$

where ΔM_x^{MR} is the difference in lateral moments from the upper to lower rotor. Mean collective, differential collective, and mean lateral controls were used to trim the net vertical force, yawing moment, and pitching moment, respectively, to zero in the body frame. Without a horizontal stabilizer modeled, mean longitudinal control was set to trim the main coaxial rotor mean hub pitching moment to zero. Finally, the differential longitudinal control was used to eliminate the difference in longitudinal $1/\text{rev}^{MR}$ flapping between the upper and lower rotors in an effort to maintain maximum blade clearance for safety.

The trim procedure was conducted across airspeeds from 80 to 240 kts at a constant 98% nominal rotor speed, consistent with flight test conditions. The rotor was not slowed to alleviate compressibility effects during flight test because

Table 3: Simulation Parameters

Airspeed	80–240 kts
Rotor Advance Ratio	0.211–0.636
Tip Mach Number (98% N_R^{MR})	0.686–0.926
Lift Offset	25%
Azimuthal Time Step	2° (180 steps)
Aerodynamic Segments / Blade	45
VVPM Particle Resolution	1–2 $\%R^{MR}$
VVPM Interference	10 chord lengths

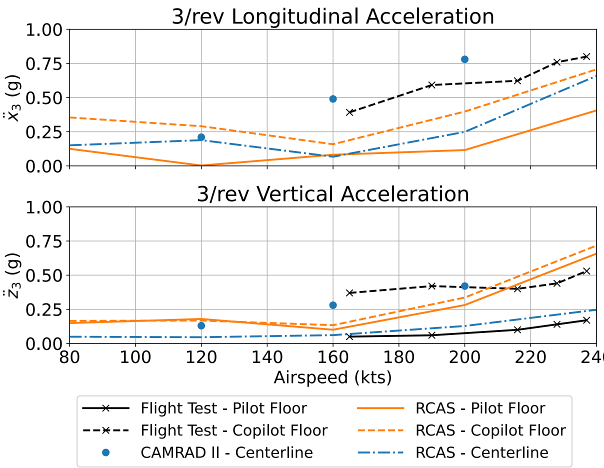

Figure 3: XH-59A Baseline Cockpit Vibrations

excessive vibration caused by airframe resonance was encountered (Ref. 8). Other simulation parameters are tabulated in Table 3, and the new extrapolated pilot and copilot floor locations were used to assess the cockpit vibrations. Fig. 3 shows the results compared to flight test data from Figure 208 in Ref. 8 and also the CAMRAD II non-extrapolated centerline predictions from Ref. 11. The discrepancy in $3/\text{rev}^{MR}$ vertical acceleration between the pilot and copilot in flight test data demonstrates the importance of accounting for roll vibrations at the cockpit; however, the present RCAS predictions don't feature a strong vibratory roll response. Instead, the slight forward offset of the floor location from the centerline node resulted in a constructive combination of pitching and vertical vibrations for both pilot and copilot seats. This reflects the same drastic vibration sensitivity to fuselage station elucidated by Mawry in Ref. 20. Furthermore, a significant vibrational yaw response at the cockpit caused a difference in pilot and copilot longitudinal $3/\text{rev}^{MR}$ vibrations. Despite the disagreement in angular vibration coupling between RCAS and flight test, extrapolating the response to the pilot and copilot seats caused vibrations to increase to more representative levels compared to the non-extrapolated centerline node response. While the CAMRAD II results show slightly better agreement with flight test data, there is no clear consensus in the literature regarding cockpit vibration levels for the 0° crossover configuration. Ruddell (Ref. 8) and Jenney (Ref. 21) both concur that roll cockpit vibrations caused different vertical responses at the pilot and copilot locations, depicted in Fig. 4a, but O'Leary (Ref. 6) stated the opposite, that vertical vibrations were identical at the two locations, depicted in Fig. 4b. Despite these inconsistencies specific to the XH-59A, the current model

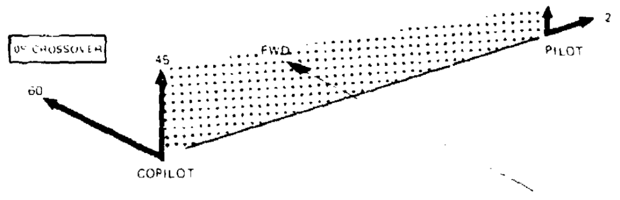

(a) Ruddell (Ref. 8)

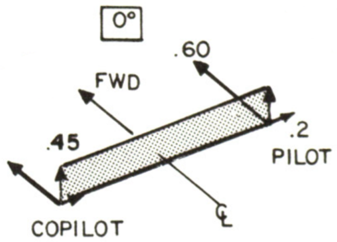

(b) O'Leary (Ref. 6)

Figure 4: Inconsistent Cockpit Vibration Flight Test Data at 200 kts.

remains a valuable tool for exploring and comparing new AVC system concepts.

MAIN COAXIAL ROTOR HHC

After trimming the aircraft, HHC pitch inputs were applied to the main coaxial rotor in an open-loop study at 200 kts, followed by a closed-loop study spanning the range of airspeeds. The HHC pitch inputs take the form

$$\theta_n = A_n \cos(n\psi_k^{MR} - \phi_n) \tag{5}$$

where

$$\psi_k^{MR} = \psi^{MR} + \frac{2\pi}{N^{MR}}(k-1) \tag{6}$$

is the k^{th} blade azimuth; n denotes the n/rev^{MR} harmonic with A_n as the amplitude and ϕ_n as the phase. The total HHC pitch is the summation of the harmonic inputs,

$$\begin{aligned} \theta_{HHC}^U &= \sum_n \theta_n^U \\ \theta_{HHC}^L &= \sum_n \theta_n^L \end{aligned} \tag{7}$$

which are superimposed onto the flight control pitch inputs,

$$\begin{aligned} \theta^U &= \theta^U + \theta_{HHC}^U \\ \theta^L &= \theta^L + \theta_{HHC}^L \end{aligned} \tag{8}$$

In the non-rotating frame, HHC actuation is mechanically constrained by the swashplate to mN^{MR}/rev^{MR} and $(mN^{MR} \pm 1)/\text{rev}^{MR}$ harmonics, where m is a positive integer (Ref. 2). For the XH-59A, which only has three blades per rotor, HHC is capable of producing every harmonic frequency, but for rotors with more than three blades, IBC is required to produce the other harmonics. However, regardless of the number of blades, if vibration control is the sole objective, the harmonics provided by HHC are the most relevant because they correspond to the rotating frame hub load frequencies that cause the non-rotating frame vibratory hub loads (Ref. 22). The other harmonics available to IBC are primarily used when there are additional objectives, such as performance improvement or noise attenuation.

Open-Loop Control

Identical $2/\text{rev}^{MR}$, $3/\text{rev}^{MR}$, and $4/\text{rev}^{MR}$ HHC inputs were applied to both upper and lower rotors at 0.5° amplitude, and the phase was swept. The hub load responses from the phase sweep are depicted in Fig. 5. All three inputs were effective in reducing the 0° crossover $3/\text{rev}^{MR}$ hub loads, each producing a single minimum less than half the baseline value. However, the $3/\text{rev}^{MR}$ thrust response opposed the $3/\text{rev}^{MR}$ hub longitudinal force and pitching moment responses, nearing a maximum above the baseline for phases where the other two are nearing minima. Therefore, a closed-loop algorithm is needed to fully evaluate the optimal vibration control authority of main coaxial rotor HHC with separate HHC inputs for upper and lower rotors.

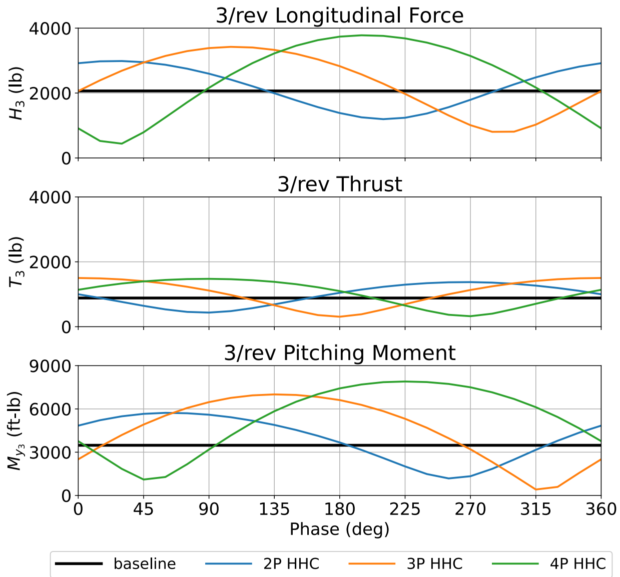

Figure 5: Open-Loop Main Coaxial Rotor HHC Effect on $3/\text{rev}^{MR}$ Hub Loads (0.5° Amplitude)

Closed-Loop Control

With the elastic fuselage modeled, the closed-loop algorithm can target vibrations at the pilot and copilot locations where accelerometers could be placed. The new Broyden trust region quasi-Newton optimization method solves a nonlinear least-squares problem (Ref. 19) where, in this case, the objective function is the summation of the squared $3/\text{rev}^{MR}$ intrusion indexes for all target locations. To account for phase, cosine and sine components of each intrusion index were treated separately, with cross terms neglected,

$$\min_{\vec{\theta}_{HHC}} \left(II_{3c}^{\text{pilot}}\right)^2 + \left(II_{3s}^{\text{pilot}}\right)^2 + \left(II_{3c}^{\text{copilot}}\right)^2 + \left(II_{3s}^{\text{copilot}}\right)^2 \quad (9)$$

where $\vec{\theta}_{HHC}$ is a vector of cosine and sine HHC control components, equivalent to specifying amplitude and phase for each harmonic input. Expanding the objective function for clarity,

$$\begin{aligned}\min_{\vec{\theta}_{HHC}} & \left(\frac{\ddot{x}_{3c}^{\text{pilot}}}{0.68}\right)^2 + \left(\frac{\ddot{y}_{3c}^{\text{pilot}}}{0.51}\right)^2 + \left(\frac{\ddot{z}_{3c}^{\text{pilot}}}{0.34}\right)^2 \\ & + \left(\frac{\ddot{x}_{3s}^{\text{pilot}}}{0.68}\right)^2 + \left(\frac{\ddot{y}_{3s}^{\text{pilot}}}{0.51}\right)^2 + \left(\frac{\ddot{z}_{3s}^{\text{pilot}}}{0.34}\right)^2 \\ & + \left(\frac{\ddot{x}_{3c}^{\text{copilot}}}{0.68}\right)^2 + \left(\frac{\ddot{y}_{3c}^{\text{copilot}}}{0.51}\right)^2 + \left(\frac{\ddot{z}_{3c}^{\text{copilot}}}{0.34}\right)^2 \\ & + \left(\frac{\ddot{x}_{3s}^{\text{copilot}}}{0.68}\right)^2 + \left(\frac{\ddot{y}_{3s}^{\text{copilot}}}{0.51}\right)^2 + \left(\frac{\ddot{z}_{3s}^{\text{copilot}}}{0.34}\right)^2\end{aligned} \quad (10)$$

In this study, $2/\text{rev}^{MR}$, $3/\text{rev}^{MR}$, and $4/\text{rev}^{MR}$ for each rotor were used independently, resulting in twelve control variables to target twelve $3/\text{rev}^{MR}$ vibration components. The stopping criterion for the optimization was such that both the pilot and copilot intrusion indexes fall below the acceptable weapons system operator threshold:

$$\max\left(II_3^{\text{pilot}},\, II_3^{\text{copilot}}\right) < 1 \quad (11)$$

The trust region is a hypersphere feasibility region that constrains the step changes in HHC controls, $\vec{\theta}_{HHC}$, throughout the optimization search to prevent nonlinear overshoot. It had an initial radius of 0.25°, which was then adapted each optimization step based on sufficient decrease and linearized model error, with an upper radial limit of 0.5°. Step size and direction were computed using Powell's dog-leg method — a hybrid of Gauss-Newton and gradient descent algorithms within the trust region (Ref. 23). The Jacobian, or transfer "T-matrix" (Ref. 24), was computed via finite differences for the initial step only, after which was is updated with Broyden rank one corrections each step to better account for nonlinearity. The progression of the optimization for each airspeed is shown in Fig. 6. The closed-loop controller performed effectively, monotonically reducing the maximum intrusion index as HHC pitch increased. This plot is also useful for deducing the vibration reduction attainable at each airspeed for any actuator given its effective pitch limit. Final maximum HHC pitch values required to reach the acceptable intrusion index threshold are plotted in Fig. 7 for multiple airspeeds.

HHC control authority initially increases with increasing airspeed, requiring less pitch, but reverses trend around 160 kts. The maximum required HHC actuation was predicted to be 2.3° at 240 kts, consistent with O'Leary's 1980 prediction (Ref. 6). Yet, this is significantly lower than the 15° predicted by Zhang et al. (Ref. 15), which is likely attributable to the change in hub loads caused by the elastic fuselage and the ease of targeting vibrations at two cockpit locations rather than the hub loads directly. The final phasors and time domain HHC pitch inputs are depicted in Fig. 8. Rotor-rotor interference, captured by the VVPM (Ref. 14), caused different optimal controls between the upper and lower rotors, especially at low advance ratio.

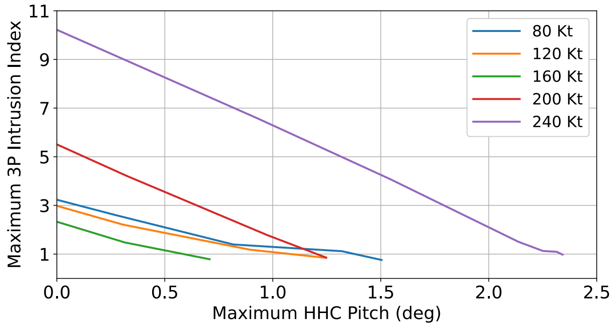

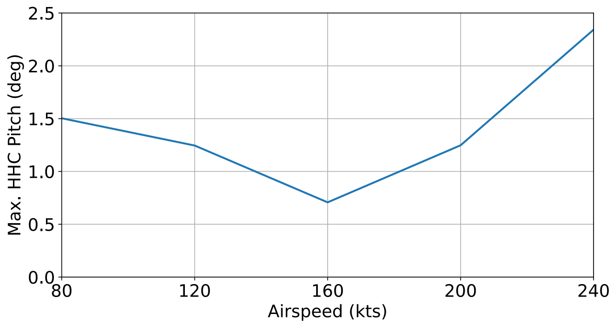

Figure 6: Main Coaxial Rotor HHC Closed-Loop Optimization Progression

Figure 7: Main Coaxial Rotor HHC Maximum Pitch Actuation Required to Reach an Intrusion Index Below 1

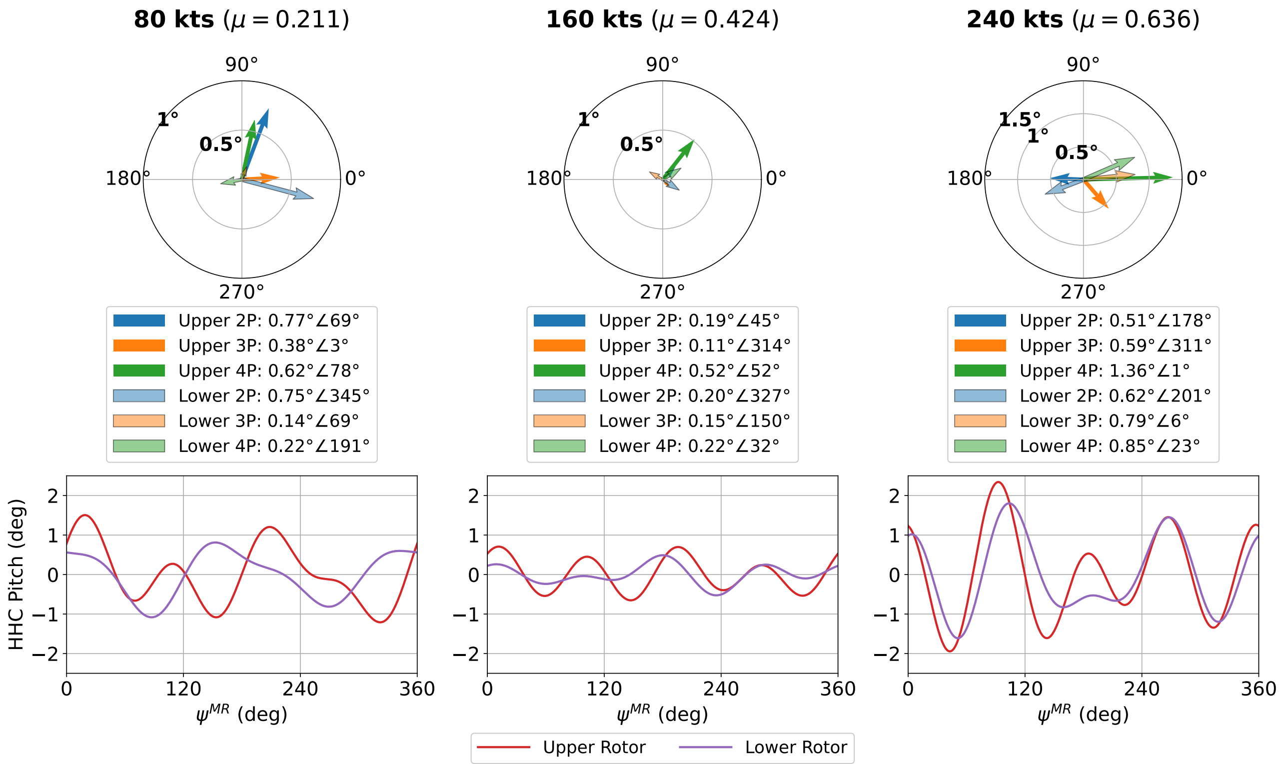

Figure 8: Main Coaxial Rotor HHC Phasors and Pitch Time Histories for 80, 160, & 240 kts

PUSHER PROPELLER AVC

Despite the demonstrated feasibility of main coaxial rotor HHC, an AVC system that is lighter, simpler, and less safety-critical is desirable. One promising alternative is pusher propeller AVC. Similar to how main coaxial rotor HHC leverages existing control surfaces, actuating the pusher propellers found on modern compound coaxial rotor vehicles for AVC could also utilize pre-existing hardware. In the event of a failure, these aircraft can continue operating without the pusher propeller after decelerating to sustainable speeds; therefore, pusher propeller AVC is less safety-critical than employing HHC or IBC on the main coaxial rotor. Furthermore, the shorter, stiffer blades of the pusher propeller should impose less stress on the AVC actuation system. A traditional swashplate with cyclic control could be used for the pusher propeller AVC, but recent developments in electro-mechanical actuators (EMAs) (Ref. 25) also offer the possibility of electrically actuated individual blade control (eIBC). The following sections first derive generalized control inputs for a pusher propeller geared at a rotation speed that is non-harmonic with respect to the main rotor. Then, pusher propeller AVC authority is explored with the RCAS XH-59A model from the main coaxial rotor HHC studies but modified with an appended pusher propeller.

Non-harmonic Pusher Propeller AVC Methodology

Conventional mN^{PP}/rev^{PP} and $(mN^{PP} \pm 1)/\text{rev}^{PP}$ HHC pitch inputs for a pusher propeller operating at a non-harmonic rotation speed to the main rotor are ineffective at cancelling fuselage vibrations caused by the main coaxial rotor because the fixed-frame pusher propeller hub loads would occur at different frequencies. Instead, a more natural methodology for pusher propeller AVC inputs is to generate additional steady fixed-frame pusher propeller hub loads with conventional collective and cyclic inputs but then modulate them with an envelope function at the desired harmonic frequency of the main coaxial rotor. Three such inputs were derived and named: modulated collective ($\theta_{0,n}$), modulated cyclic sine ($\theta_{1s,n}$), and modulated cyclic cosine ($\theta_{1c,n}$),

$$\theta_{0,n} = A_{0,n}\cos(n\Omega^{MR}t - \phi_n) \tag{12}$$

$$\theta_{1s,n} = A_{1s,n}\sin(\psi_k^{PP})\cos(n\Omega^{MR}t - \phi_n) \tag{13}$$

$$\theta_{1c,n} = A_{1c,n}\cos(\psi_k^{PP})\cos(n\Omega^{MR}t - \phi_n) \tag{14}$$

where

$$\psi_k^{PP} = \psi^{PP} + \frac{2\pi}{N^{PP}}(k-1) \tag{15}$$

For this modulating envelope function, time is denoted by t, rather than an azimuthal time reference, to emphasize that it is not spatially dependent on blade azimuth. These controls are then summed,

$$\theta_{AVC}^{PP} = \sum_n \theta_{0,n}^{PP} + \theta_{1s,n}^{PP} + \theta_{1c,n}^{PP} \tag{16}$$

and superimposed onto the constant collective pitch, θ_0^{PP}, used to trim the pusher propeller,

$$\theta^{PP} = \theta_0^{PP} + \theta_{AVC}^{PP} \tag{17}$$

Steady thrust and moments are modulated with the $\cos(n\Omega^{MR}t - \phi_n)$ envelope function, but vibratory torque and in-plane forces are also generated due to the pusher propeller operating in axial flow with large blade pitch and inflow angles. The modulation of the collective input also generates vibratory torque, and the modulation of the cyclic inputs also generate vibratory in-plane forces, all at the same envelope function frequency. These controls are analogous to some of the oscillating swashplate inputs used to excite structural modes in tiltrotor aeroelastic stability testing (Ref. 26).

For a rigid pusher propeller with N^{PP} blades, theoretical non-rotating frame vibratory hub loads were calculated from representative rotating-frame hub forces and moments per blade (Ref. 22).

Modulated Collective

$$\begin{aligned} T_n &= \sum_{k=1}^{N^{PP}} S_{z_0}\cos(n\Omega^{MR}t + \phi_n) \\ &= N^{PP} S_{z_0}\cos(n\Omega^{MR}t + \phi_n) \end{aligned} \tag{18}$$

$$\begin{aligned} Q_n &= \sum_{k=1}^{N^{PP}} N_{L_0}\cos(n\Omega^{MR}t + \phi_n) \\ &= N^{PP} N_{L_0}\cos(n\Omega^{MR}t + \phi_n) \end{aligned} \tag{19}$$

Modulated Cyclic Sine

$$\begin{aligned} M_{x_n} &= \sum_{k=1}^{N^{PP}} N_{F_1}\sin(\psi_k^{PP})\cos(n\Omega^{MR}t + \phi_n)\sin(\psi_k^{PP}) \\ &= \frac{N^{PP}}{2} N_{F_1}\cos(n\Omega^{MR}t + \phi_n) \end{aligned} \tag{20}$$

$$\begin{aligned} H_n &= \sum_{k=1}^{N^{PP}} S_{x_1}\sin(\psi_k^{PP})\cos(n\Omega^{MR}t + \phi_n)\sin(\psi_k^{PP}) \\ &= \frac{N^{PP}}{2} S_{x_1}\cos(n\Omega^{MR}t + \phi_n) \end{aligned} \tag{21}$$

Modulated Cyclic Cosine

$$\begin{aligned} M_{y_n} &= \sum_{k=1}^{N^{PP}} N_{F_1}\cos(\psi_k^{PP})\cos(n\Omega^{MR}t + \phi_n)\cos(\psi_k^{PP}) \\ &= \frac{N^{PP}}{2} N_{F_1}\cos(n\Omega^{MR}t + \phi_n) \end{aligned} \tag{22}$$

$$\begin{aligned} Y_n &= \sum_{k=1}^{N^{PP}} S_{x_1}\cos(\psi_k^{PP})\cos(n\Omega^{MR}t + \phi_n)\cos(\psi_k^{PP}) \\ &= \frac{N^{PP}}{2} S_{x_1}\cos(n\Omega^{MR}t + \phi_n) \end{aligned} \tag{23}$$

The remaining AVC load calculations for each input, omitted for conciseness, reduced to zero.

For each calculation, the modulating envelope function does not depend on blade index, k, so it was moved outside of the summation. Trigonometric identities were then used to decompose the multiplication of two $1/\text{rev}^{PP}$ terms into a steady term and a $2/\text{rev}^{PP}$ term, each with half the magnitude. The steady term was moved outside of the summation, but the pusher propeller filters out the $2/\text{rev}^{PP}$ term, as long as the pusher propeller has more than two blades. Thus, the resulting fixed-frame hub loads will only retain the n/rev^{MR} harmonic from the modulating envelope function, which will be exploited to counter the vibrations from the main coaxial rotor.

Modified XH-59A Model with Pusher Propeller

To test the practical application of non-harmonic pusher propeller AVC, a pusher propeller resembling that of the Sikorsky S-97 Raider® was designed due to its similar weight-class and configuration to the XH-59A. The propeller is depicted in Fig. 9, and its specifications are listed in Table 4. A rotation speed of 5.5 times that of the main rotor was selected because it is a simple non-harmonic ratio that remains periodic over two main rotor revolutions. This allows for easier RCAS implementation.

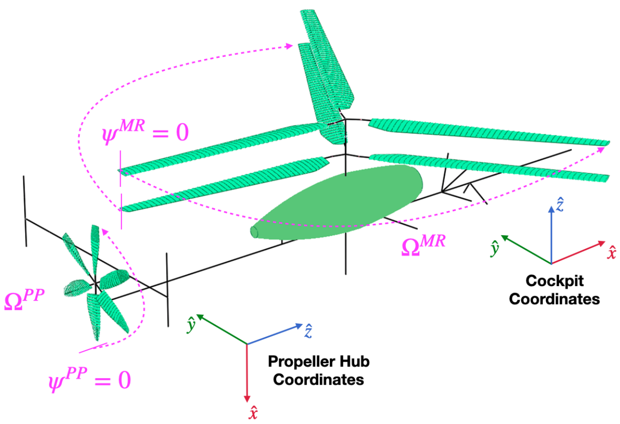

Figure 9: Modified XH-59A RCAS Model with Added Pusher Propeller

The pusher propeller was positioned in line with the center of gravity (CG) to avoid producing a steady pitching moment. Its thrust was used to offset the total drag, of which the fuselage drag was modeled with an effective flat plate

Table 4: Pusher Propeller Specifications

Number of Blades	6
Diameter	8 ft
Twist	$-46°$
Nominal Rotation Speed	1897.5 RPM ($5.5 \times N_R^{MR}$)
VVPM Particle Resolution	2.5–5 $\%R^{PP}$
VVPM Interference	20 chord lengths

area of 19.41 ft^2, 10% less than the measured XH-59 value of 21.57 ft^2 to account for modern hub fairings (Ref. 10). Paired with the same main coaxial rotor trim procedure, the propeller was trimmed up to 200 kts; the resulting control angles are shown in Fig. 10. The propeller rotating counter clockwise ($-\hat{z}$ in its hub coordinates) produced a steady torque that was balanced by an increase in main coaxial rotor mean lateral control, altering the trim compared to the original XH-59A model.

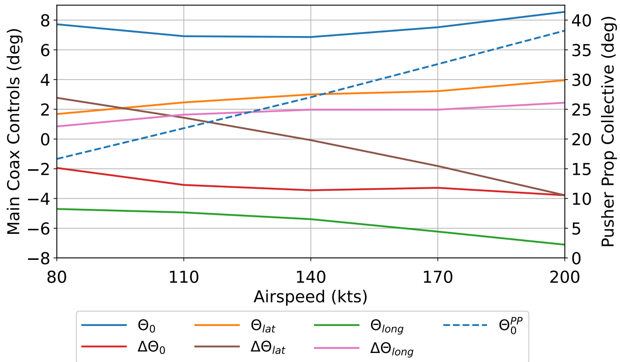

Figure 10: Modified XH-59A Trim

Pusher propeller AVC was evaluated in four stages, all at 200 kts. First, the pusher propeller was isolated and AVC-induced hub loads were compared between blade element momentum theory (BEMT) and the VVPM. Second, the pusher propeller was coupled with the elastic fuselage but with the main coaxial rotor aerodynamics disabled, allowing the sensitivity of cockpit vibrations to pusher propeller AVC, as the sole source of excitation, to be evaluated. Third, open-loop sweeps of control phase and amplitude were conducted. Fourth, closed-loop control actuation requirements were predicted.

Isolated Propeller AVC Airloads

To validate the pusher propeller AVC theoretical hub loads calculated in Eqs. (18)–(23), each control input was applied individually with 1° amplitude to the standalone pusher propeller model at 200 kts. In addition to the mid-fidelity VVPM aerodynamic model, BEMT was also used for a low-fidelity comparison. For the VVPM, the pusher propeller collective was set to the value from the full-vehicle trim; for BEMT, it was trimmed to the same thrust. Results are depicted in Fig. 11 over a duration equal to two revolutions of the main rotor. Evident by the dashed-lines for BEMT, the pusher propeller AVC inputs produced the expected hub loads at the desired frequency of $3/\text{rev}^{MR}$, with directionality consistent with prediction. The VVPM also showed good agreement, though it caused additional smaller $3/\text{rev}^{MR}$ loads in some directions that reduced to zero in the simple theoretical calculations. Nonetheless, these results confirm that the beating rotating-frame hub loads are filtered and that this non-harmonic pusher propeller AVC approach can produce three independent non-rotating frame hub load responses at the single desired frequency of N^{MR}/rev^{MR}.

Pusher Propeller AVC Fuselage Sensitivity

Next, the pusher propeller was integrated into the full-aircraft model by connecting it to the elastic fuselage. To isolate the fuselage response caused by pusher propeller AVC, the main coaxial rotor aerodynamics were disabled but with the blades still structurally modeled and spinning. The same series of 1° amplitude AVC inputs was applied to the pusher propeller, and the resulting time histories of pilot and copilot floor accelerations are plotted in Fig. 12. As expected from the previous isolated-propeller case, the generated $3/\text{rev}^{MR}$ pusher propeller hub loads excited a fuselage response at the same desired frequency of N^{MR}/rev^{MR}. Notably, the modulated cyclic controls produced greater longitudinal and lateral cockpit accelerations than the modulated collective control. This is because the extrapolated cockpit floor locations are sensitive to fuselage bending modes, which manifest as rotational vibrations about the centerline node from which the extrapolated locations originate. At 200 kts, the largest cockpit acceleration response was in the cockpit longitudinal direction, while the vertical response was the smallest.

Open-Loop Control

With confirmation that pusher propeller AVC can generate a fuselage response at arbitrary frequency, the main coaxial rotor aerodynamics were re-enabled. Open-loop phase and amplitude sweeps were then conducted to study the effects on $3/\text{rev}^{MR}$ cockpit vibrations at the pilot and copilot floor locations, quantified by the $3/\text{rev}^{MR}$ component of the intrusion index. The phase sweep, performed using 1° amplitude for each control, is shown above the amplitude sweep in Fig. 13. The responses at the pilot and copilot floor locations were nearly in phase for the modulated collective and cyclic cosine controls, so a phase could be selected to reduce both intrusion indexes simultaneously. In contrast, the modulated cyclic sine response was about 90° out of phase between the two locations and exhibited minimal control authority over copilot floor vibrations. Its phase was therefore selected to reduce the pilot floor vibrations. Based on these results, the following control phases were selected for the amplitude sweep: 290° for modulated collective, 135° for modulated cyclic sine, and 110° for modulated cyclic cosine. The amplitude sweep revealed that modulated cyclic cosine had the greatest initial control authority over copilot floor vibrations, but its effectiveness tapered at higher amplitudes, reaching a minimum $3/\text{rev}^{MR}$ intrusion index of 4.1 at 3.4°. The modulated collective control continued reducing vibrations past that point; however, the slope of the pilot floor response flattened considerable by 5° amplitude and would likely not reach the accept-

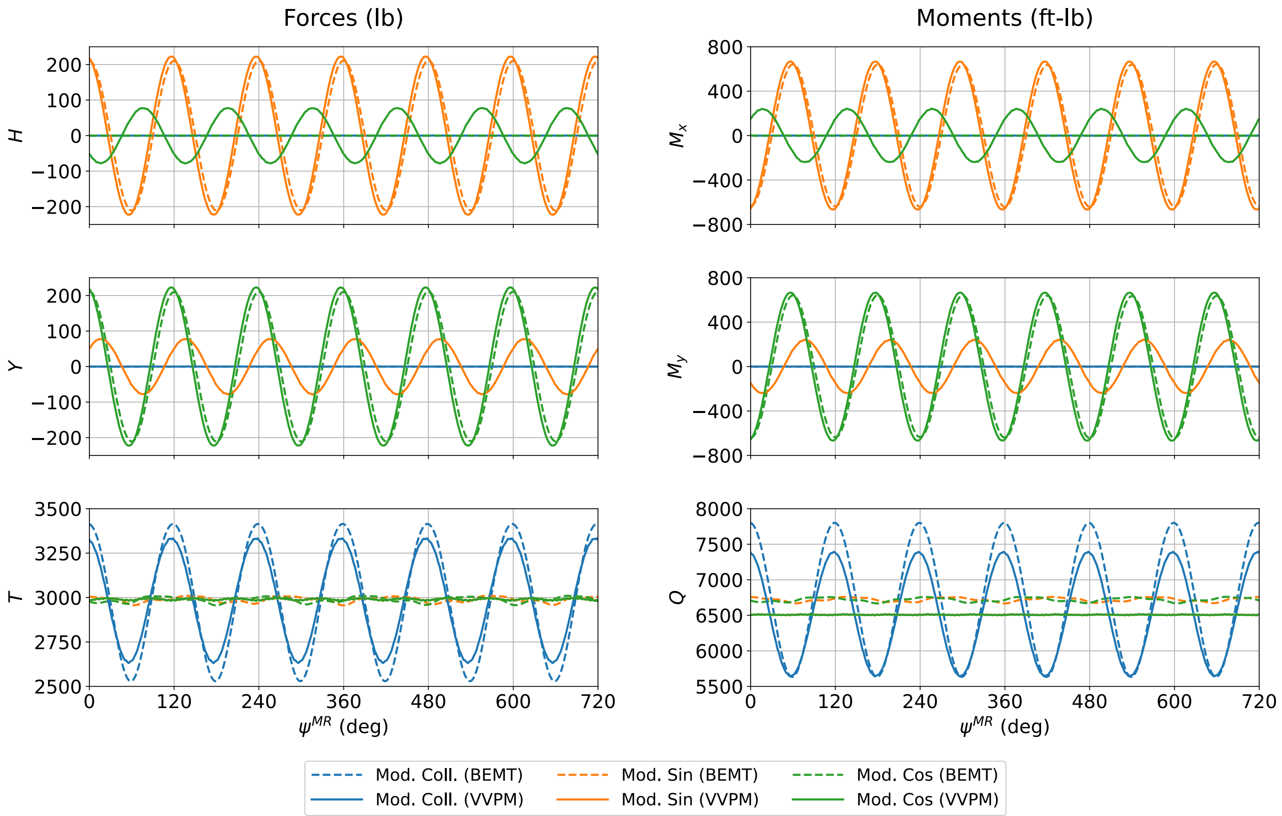

Figure 11: Isolated Pusher Propeller AVC: Non-Rotating Hub Loads at 200 kts with 1° Amplitude AVC Inputs.

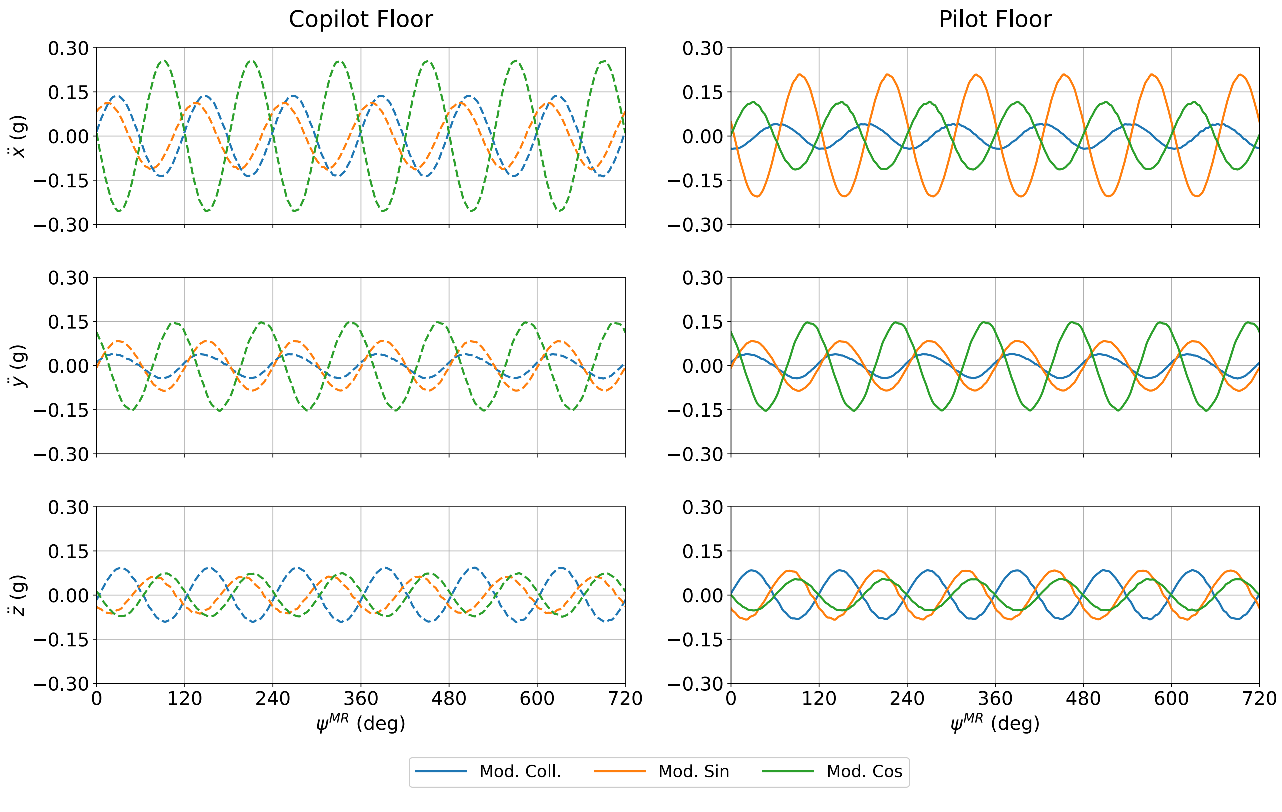

Figure 12: Coupled Pusher Propeller AVC - Elastic Fuselage: Cockpit Floor Accelerations Induced by 1° Amplitude AVC Inputs at 200 kts. Main coaxial rotor aerodynamics were disabled to isolate the effects of pusher propeller AVC.

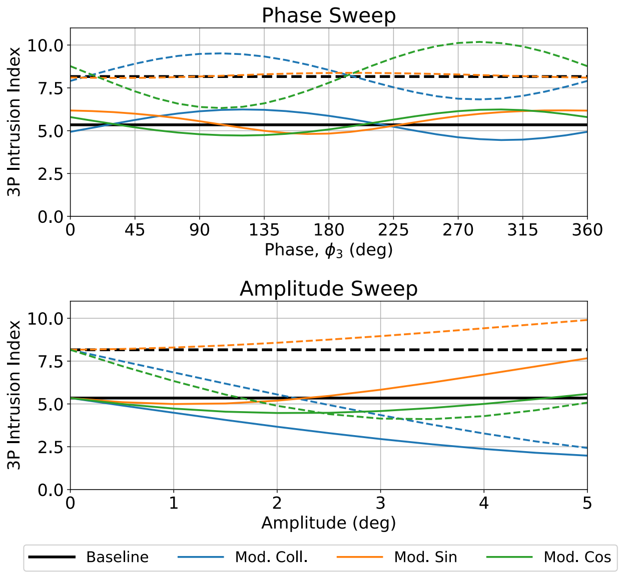

Figure 13: Open-Loop Pusher Propeller AVC Effects on Pilot and Copilot Floor $3/\text{rev}^{MR}$ Intrusion Indexes at 200 kts

able intrusion index level of 1, even with unfeasible, excessive amplitude. Finally, the modulated cyclic sine control slightly decreased the pilot floor vibrations, but beyond 1° amplitude, it caused a sharp increase in copilot floor vibrations. Thus, closed-loop control is needed to optimally combine these controls to achieve the most effective vibration reduction across both cockpit floor locations.

Closed-Loop Control

For closed-loop pusher propeller AVC, the same Broyden trust region quasi-Newton optimization algorithm and objective function from Eq. (10) were employed, but this time with the pusher propeller AVC inputs, decomposed into a total of six cosine and sine components. The progression of this optimization is depicted in Fig. 14. Notably, around 4° pitch, the pilot floor $3/\text{rev}^{MR}$ intrusion index began to plateau, but the optimizer adapted to further reduce overall vibrations. Near the acceptable intrusion index threshold of 1, the maximum pusher propeller AVC pitch reached 4.8°. The optimized control amplitudes and phases, along with the AVC pitch time histories, are plotted in Fig. 15. While modulated collective was the dominant control, its combination with lower amplitude modulated cyclic inputs was more effective at reducing the $3/\text{rev}^{MR}$ vibrations at both cockpit locations, with less AVC pitch actuation than the standalone open-loop modulated collective result in Fig. 13.

CONCLUSIONS & FUTURE WORK

This paper represents a transition point in the ongoing development of AVC for main coaxial rotor compound vehicles. Building on prior work focused on main coaxial rotor HHC, several advancements were made:

- Model fidelity was significantly improved: the aerodynamic model was upgraded to the VVPM, elastic fuselage responses were extrapolated to match flight test measurement locations, vibrations were quantified with intrusion index components, and a more robust nonlinear optimization algorithm was implemented for closed-loop control.

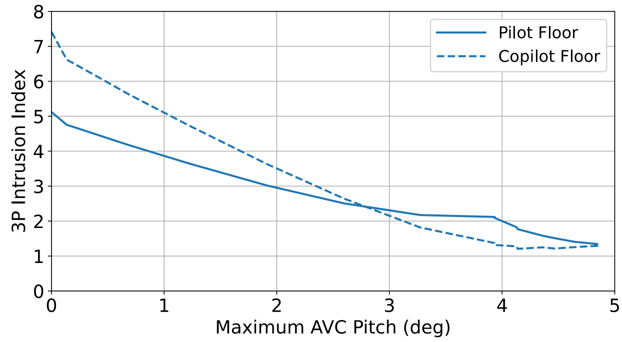

Figure 14: Closed-Loop Pusher Propeller AVC Optimization Progression at 200 kts

- Pilot and copilot floor vibrations levels were validated, despite inconsistencies in available flight test literature. The updated RCAS model, with extrapolated responses, predicted vibrations magnitudes comparable to flight test data, albeit with inconclusive trends between pilot and copilot floor locations.
- Main coaxial rotor HHC authority was assessed with both open and closed-loop analyses that predicted a maximum HHC pitch amplitude requirement of 2.3° at 240 kts to achieve an acceptable intrusion index below 1 at both cockpit locations.

Pusher propeller AVC was then introduced as an alternative lighter, simpler, and less safety-critical AVC system, utilizing non-harmonic excitation:

- Non-rotating frame pusher propeller hub loads were successfully generated at an arbitrary frequency for each of the modulated collective, modulated cyclic sine, and modulated cyclic cosine controls.
- Pusher propeller AVC was demonstrated to be capable of exciting the elastic fuselage at $3/\text{rev}^{MR}$, revealing that the cockpit longitudinal acceleration was the most sensitive, while vertical acceleration was the least.
- Open and closed-loop studies predicted large required pusher propeller AVC pitch amplitudes for cockpit vibration reduction. At 200 kts, a maximum pitch amplitude of 4.8° was required to reach near-acceptable intrusion index levels.

Future improvements to the closed-loop control strategies for both AVC systems could proceed along two main paths. First, the AVC pitch amplitude could also be minimized directly within the objective function, by incorporating weighted control terms, or limited with a penalty method (Refs. 23, 24). This may help reduce the required AVC pitch actuation to make both systems more mechanically feasible. If the required AVC pitch amplitude still exceeds actuator limits, a hybrid approach combining main coaxial rotor HHC and pusher propeller AVC may prove more

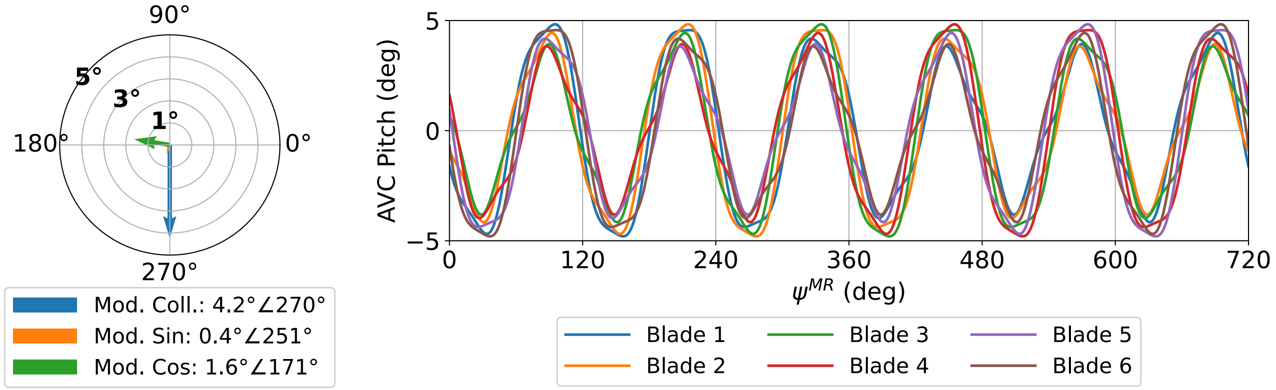

Figure 15: Closed-Loop Pusher Propeller AVC Optimized Pitch at 200 kts

efficient. Second, expanding the set of fuselage sensors beyond the two cockpit floor locations may help reduce the vibrations everywhere throughout the airframe. For main coaxial rotor HHC, this would indirectly target the main coaxial rotor vibratory hub loads; however, while pusher propeller AVC was shown to decrease the vibrations at the cockpit, it might have also excited larger vibrations elsewhere in the fuselage. This highlights a major difference between the two systems. The former can combat vibrations at their origin — the higher harmonic airloads on the main coaxial rotor blades — whereas the latter acts on a different rotating system, separated by the fuselage, and is expected to have limited influence on the main coaxial rotor airloads. Increasing the number of fuselage sensors may also raise the required AVC pitch amplitudes for both systems, but likely more so for pusher propeller AVC than for main coaxial rotor HHC.

Pusher propellers themselves are a known source of fuselage vibration, due to aerodynamic interaction with both the main rotor and airframe wakes, the latter of which can actually increase pusher propeller efficiency (Refs. 27, 28). While the VVPM captured some periodic aerodynamic interference from the main coaxial rotor to the pusher propeller, those effects were not explicitly analyzed in this work. Moreover, the unsteady hub wake was not modeled, which can impact the pusher propeller and cause additional vibration (Ref. 29). Although these aerodynamic interference effects may complicate the implementation of pusher propeller AVC, they underscore its multi-functional potential: such a system could reduce unsteady airloads at the pusher propeller while simultaneously mitigating fuselage vibrations directly from the main coaxial rotor. For these reasons, pusher propeller AVC merits further investigation.

ACKNOWLEDGMENTS

The authors thank Dr. Jae-Sang Park from Chungnam University for providing the XH-59A elastic fuselage model. Additionally, the authors thank Dr. Louis Centolanza, Dr. Hyeonsoo Yeo, Dr. Mark Fulton, and Dr. Joon Lim from the U.S. Army Combat Capabilities Development Command, as well as Mr. William A. Welsh from Sikorsky Aircraft, A Lockheed Martin Company. The authors also thank Advanced Rotorcraft Technology, Inc. for their guidance with RCAS and the VVPM.

This research is funded by the U.S. Government under Cooperative Agreement No. W911W6-21-2-0002. The U.S. Government is authorized to reproduce and distribute reprints for Government purposes notwithstanding any copyright notation thereon. The views and conclusions contained in this document are those of the authors and should not be interpreted as representing the official policies or position, either expressed or implied, of the U.S. Army Combat Capabilities Development Command (DEVCOM), Aviation & Missile Center (AvMC), or the U.S. Government.

REFERENCES

1. Blackwell, R., and Millott, T., "Dynamics Design Characteristics of the Sikorsky X2 Technology™ Demonstrator Aircraft," American Helicopter Society 64th Annual Forum Proceedings, Montreal, Canada, April 29–May 1, 2008.

2. Kessler, C., "Active rotor control for helicopters: motivation and survey on higher harmonic control," 36th European Rotorcraft Forum Proceedings, Paris, France, September 7–9, 2010.

3. Kessler, C., "Active rotor control for helicopters: individual blade control and swashplateless rotor designs," *CEAS Aeronautical Journal*, Vol. 1, (1), Presented at the 36th European Rotorcraft Forum in 2010, May 2011, pp. 23–54. DOI: 10.1007/s13272-011-0001-0.

4. Stewart, W., "Second Harmonic Helicopter Control on the Rotor," Reports and Memoranda R. & M. 2997, Aeronautical Research Council, London, 1952.

5. Roth, D., "Advanced Vibration Technology by IBC Technology," 30th European Rotorcraft Forum Proceedings, Marseille, France, September 14–16, 2004.

6. O'Leary, J., and Miao, W., "Design of Higher Harmonic Control for The ABC™," American Helicopter Society Mideast Region National Specialists' Meeting on Rotor System Design, October 22–24, 1980.

7. Jacobellis, G., *Improvement of High-Speed Coaxial Rotor Performance Using Redundant Controls and Camber Morphing*, Ph.D. thesis, Rensselaer Polytechnic Institute, December 2018.

8. Ruddell, A. J., “Advancing Blade Concept (ABC) Technology Demonstrator,” Technical Report 81-D-5, US AVRADCOM, May 1981.

9. Ruddell, A. J., “XH-59A (ABC) Technology Demonstrator Altitude Expansion and Operational Tests,” Technical Report 81-D-35, US AVRADCOM, December 1981.

10. Felker, F. F., III, “Performance and Loads Data from a Wind Tunnel Test of a Full-Scale, Coaxial, Hingeless Rotor Helicopter,” Technical Report 81-A-27, US AVRADCOM, October 1981.

11. Lee, Y.-L., Kim, D.-H., Park, J.-S., and Hong, S.-B., “Vibration reduction simulations of a lift-offset compound helicopter using two active control techniques,” *Aerospace Science and Technology*, Vol. 106, (106181), November 2020. DOI: https://doi.org/10.1016/j.ast.2020.106181.

12. Beyer, J. A., Smith, E. C., Schmitz, S. U., and Zhang, J., “Individual Blade Pitch Control (IBC) for Vibration Reduction of Lift-Offset Coaxial Rotor Vehicles with Auxiliary Propulsion,” Vertical Flight Society 79$^{\text{th}}$ Annual Forum Proceedings — West Palm Beach, FL, May 16–18, 2023.

13. He, C., and Zhao, J., “Modeling Rotor Wake Dynamics with Viscous Vortex Particle Method,” *AIAA Journal*, Vol. 47, (4), April 2009, pp. 902–915. DOI: 10.2514/1.36466.

14. Kim, J., Hasbun, M., Saberi, H., He, C., and Bhagwat, M. J., “RCAS, VVPM, and Panel Coupling Enhancements for Interference and Downloads Prediction,” Vertical Flight Society 77$^{\text{th}}$ Annual Forum Proceedings, Virtual, May 10–4, 2021.

15. Zhang, J., Smith, E. C., and Schmitz, S. U., “Vibration Reduction Using Individual Pitch Controls for Lift-Offset Coaxial Rotor Vehicles at Low and High Speeds,” Vertical Flight Society 6$^{\text{th}}$ Decennial Aeromechanics Specialists’ Conference Proceedings, Santa Clara, CA, February 6–8, 2024.

16. Mawry, I. R., Smith, E. C., Schmitz, S. U., Zhang, J., and Park, J.-S., “Fuselage Vibration Reduction of Lift-Offset Coaxial Rotor Vehicles with Auxiliary Propulsion via Individual Blade Pitch Control (IBC),” 50$^{\text{th}}$ European Rotorcraft Forum Proceedings, Marseille, France, September 9–12, 2024.

17. Cole, L. H., “Front view of an XH-59A Advancing Blade Concept (ABC) rotor system aircraft in flight at the Marine Corps Development and Education Command Air Facility,” Marine Corps Base Quantico, VA, *Combined Military Service Digital Photographic Files*, U.S. National Archives and Records Administration, NAID: 6378163, November 3, 1981.

18. Crews, S. T., Lewis, W. D., and Dulaney, K. E., “Requirements for Rotorcraft Vibration Specifications, Modeling, and Testing,” Technical Report ADS-27A-SP, U.S. Army AMCOM, May 2006.

19. Zeng, M., and Fu, H., “A Broyden Trust Region Quasi-Newton Method for Nonlinear Equations,” *IAENG International Journal of Computer Science*, Vol. 46, August 2019, pp. 454.

20. Mawry, I. R., *Fuselage Vibration Reduction of Lift-Offset Coaxial Rotor Vehicles with Auxiliary Propulsion via Individual Blade Pitch Control*, Master’s thesis, The Pennsylvania State University, December 2024.

21. Jenney, D. S., “ABC$^{\text{TM}}$ Aircraft Development Status,” 6$^{\text{th}}$ European Rotorcraft Forum Proceedings, Bristol, England, September 16–19, 1980.

22. Johnson, W., *Rotorcraft Aeromechanics*, Cambridge Aerospace Series, Cambridge University Press, 2013, pp. 620, 718–720.

23. Nocedal, J., and Wright, S. J., *Numerical Optimization*, Springer Science & Business Media, second edition, 2006, pp. 66–98.

24. Davis, M. W., “Refinement and Evaluation of Helicopter Real-Time Self-Adaptive Active Vibration Controller Algorithms,” Contractor Report NASA-CR-3821, United Technologies Research Center; NASA, East Hartford, CT, United States, August 1984.

25. Arnold, U. T. P., and Haar, J., “Design and Testing of a Highly Redundant Electro-Mechanical Actuator for Aircraft Primary Flight Control Applications,” Vertical Flight Society 80$^{\text{th}}$ Annual Forum Proceedings, Montréal, Canada, May 7–9, 2024.

26. Kreshock, A. R., Thornburgh, R., and Wilbur, M., “Overview of the TiltRotor Aeroelastic Stability Testbed,” AIAA SCITECH 2022 Forum, San Diego, CA, January 3–7, 2022. DOI: 10.2514/6.2022-0566.

27. Schuster, D., “S-97 Raider® Propulsor Flight Loads and Validation,” Vertical Flight Society 79$^{\text{th}}$ Annual Forum Proceedings, West Palm Beach, FL, May 16–18, 2023.

28. Min, B.-Y., Moffitt, B., Bowles, P. O., Wake, B. E., and Lorber, P. F., “Analysis and Experimental Testing of S-97 Raider® Propeller,” American Helicopter Society Aeromechanics Design for Transformative Vertical Flight Technical Meeting Proceedings, San Francisco, CA, May 2021.

29. Schmitz, S. U., Jaffa, N., Reich, D., Nickels, A., Pabon, R., Piqué, A., and Durachko, T., “Flow Diagnostics of Scaled-Model Coaxial Rotor Hub Flows,” Vertical Flight Society 80$^{\text{th}}$ Annual Forum Proceedings, Montréal, Canada, May 7–9, 2024.